Supporting Information

Nitrogen Doping–Enabled Low-Temperature Capacitance Retention in Carbon Materials

Anica B. Pinongcos[1], Xinzhe Xue[1], Megan C. Freyman[2], Seongkoo Cho[2], Swetha Chandrasekaran[2], Qiu Ren[1], Nathan Delaney[1], Emma Coester[1], Marissa Wood[2], Marcus A. Worsley[2,*], and Yat Li[1,*]

[1] Department of Chemistry and Biochemistry, University of California Santa Cruz, 1156 High Street, Santa Cruz, California 95064, USA

[2] Lawrence Livermore National Laboratory, 7000 East Avenue, Livermore, California 94550, USA

E-mail: worsley1@llnl.gov; yatli@ucsc.edu

Experimental Section

Preparation of nitrogen-doped multiscale porous carbon aerogel electrode (N-MCA)

SiO_2 nanospheres (300 μm) were synthesized via a modified Stöber method.[1,2] One gram of SiO_2 nanospheres were sonicated and dispersed in 2 mL of Milli-Q water for 24 h in an ice-water bath. The dispersion was then mixed with 1 g of CNC powder and 2 mL of Milli-Q water in a planetary Thinky mixer at 2000 rpm.

The resulting viscous ink was cast into a silicon-based mold, frozen in dry ice for 30 min, and then freeze-dried under vacuum for 48 h. The cellulose-SiO_2 aerogels were carbonized in a tube furnace at 800 °C for 2 h under N_2 (40 standard cubic centimeter per minute (sccm)) with a ramp rate of 5 °C/min. Macropores were introduced by soaking the carbonized samples in 4 M NaOH at 80 °C for 2 days to dissolve the SiO_2, followed by immersion in water at 80 °C overnight to remove residual NaOH and silicate salts. The samples were then dried at 80 °C for 2 h, immersed in 1 M KOH for 8 h, dried again at 80 °C for at least 2 h, and then re-annealed at 800 °C for 1 h under N_2 (40 sccm, 5 °C/min). After cooling to room temperature, the samples were immediately washed with 0.5 M HCl, rinsed with water until a neutral pH was measured, and dried at 80 °C overnight. Nitrogen doping was achieved via ammonia treatment. The samples were annealed at elevated temperatures (ranging from 700 °C to 1000 °C) for 10 min under a NH_3/N_2 mixture (NH_3: 10 sccm; N_2: 50 sccm, 5 °C/min), followed by 110 min under N_2 at the same temperature. The samples were then cooled down naturally to room temperature. For comparison, undoped multiscale porous carbon aerogels (MCA) were prepared using the same procedure but without the ammonia treatment.

Material Characterization

Morphology and elemental distribution of the electrodes were analyzed with scanning electron microscopy (SEM), scanning transmission electron microscopy (STEM), and energy-dispersive spectroscopy (EDS) using Thermo Scientific Scios 2 DualBeam equipped with an Oxford Instruments AZtecLive Ultim Max 100 EDS detector. The surface chemical composition of the functional groups was investigated by X-ray photoelectron spectroscopy (XPS, Nexus X-ray Photoelectron Spectrometer) using monochromatic Al Kα X-ray (1486.6 eV) with 400 μm spot size. Nitrogen sorption isotherms were measured using an Autosorb iQ after degassing samples at 110 °C under vacuum for 10 h. Specific surface area and pore-size distribution were determined by Brunauer-Emmett-Teller (BET) and Barrett-Joyner-Halenda (BJH) methods.

Contact Angle Measurements

Contact angle measurements were performed using the Ossila Contact Angle Goniometer instrument. The minimum frame duration for the contact angle video was set to 0.03 second.

Electrochemical Characterization

Electrochemical measurements were performed in a three-electrode configuration using electrochemical stations (BioLogic EC-Lab SP-300 and VMP-3e) inside an Ar gas-filled glovebox. The doped and undoped MCA with geometric areas of 0.79 cm^2 were used as working electrodes. Pt/Pt^+ and carbon paper were used as the pseudo-reference electrode and the counter electrode, respectively. In nonaqueous electrolytes such as 1 M $TEABF_4$ in acetonitrile/methyl formate (ACN/MF), metallic Pt rapidly establishes a surface Pt/Pt^+ redox equilibrium, providing a stable and reproducible potential without introducing additional ions into the system. This

approach could prevent contamination in the electrolyte due to the chemical inertness of Pt. Symmetric devices were fabricated in a coin cell by assembling two pieces of identical carbon aerogels, separated by a 16 mm diameter glass microfiber filter (Whatman 1820-125 GF/A, 1.6μm). Each electrode for the device was sandwiched between two Ni-foam sheets to ensure good electrical contact. The total mass loading of the electrodes is approximately 13.1 mg cm^{-2}, and the thickness of each electrode is about 0.5 mm. The electrolyte used for all the electrochemical testing was a 0.5 M tetraethylammonium tetrafluoroborate ($TEABF_4$) solution in a 1:1 (v/v) mixture of acetonitrile (AN) and methyl formate (MF). Long-term stability tests of the coin cells at -40 °C were conducted using a dry-ice bath prepared from an ethanol/H_2O mixture (4:1 v/v). The cells were cycled at a current density of 50 mA cm^{-2} within a voltage window of 0-2.2 V.

Calculations

The gravimetric capacitance ($C_{G,}$ F g^{-1}) of a single electrode was calculated based on the galvanostatic charging and discharging (GCD) curves using Eq. 1:

$$C_G = \frac{I \times t}{\Delta U \times m} \quad \text{(Eq. 1)}$$

where I is the current (mA), t is the discharge time (s), ΔU is the potential window excluding the iR drop, and m is the mass (mg).

The volumetric capacitance (C_V, mF cm^{-3}) of the symmetric device was calculated as:

$$C_V = \frac{I \times t}{\Delta U \times V} \quad \text{(Eq. 2)}$$

where V is the total volume of the two electrodes (cm^3).

The volumetric energy density (E, Wh L^{-1}) and power density (P, W L^{-1}) of the symmetric supercapacitor device were calculated using the following equations:

$$E_V = \frac{C_V \Delta U^2}{2 \times 3600} \quad \text{(Eq.3)}$$

$$P_V = \frac{E_V \times 3600}{t} \quad \text{(Eq. 4)}$$

Kinetic Analysis

Charge storage kinetics were evaluated by relating the current response (*i*) to the sweep rate (ν) extracted from the cyclic voltammetry (CV) curves: log *i*= *b* log ν + k. A *b* value of 1 indicates ideal capacitive behavior, while a *b* value of 0.5 indicates a diffusion-controlled storage process. The Trasatti method was employed to quantify the relative contributions from surface capacitance ($C_{NON\text{-}DIFFUSION}$) and bulk capacitance ($C_{DIFFUSION}$).[3,4] Areal capacitances (*C*) at different scan rates were calculated from:

$$C = \frac{S_{CV}}{2v\,\Delta U} \quad \text{(Eq.5)}$$

where S_{CV} is the integrated area under the CV curve (mA V cm^{-2}). For slow scan rates (1–5 mV s^{-1}), *C* was plotted against $v^{-1/2}$ and extrapolation to $v \rightarrow +\infty$ (y-intercept) yields $C_{NON\text{-}DIFFUSION}$. $C_{DIFFUSION}$ was then determined from $C_{TOTAL} - C_{NON\text{-}DIFFUSION}$, allowing the percentage contributions from each mechanism to be calculated.

Supplementary Figures

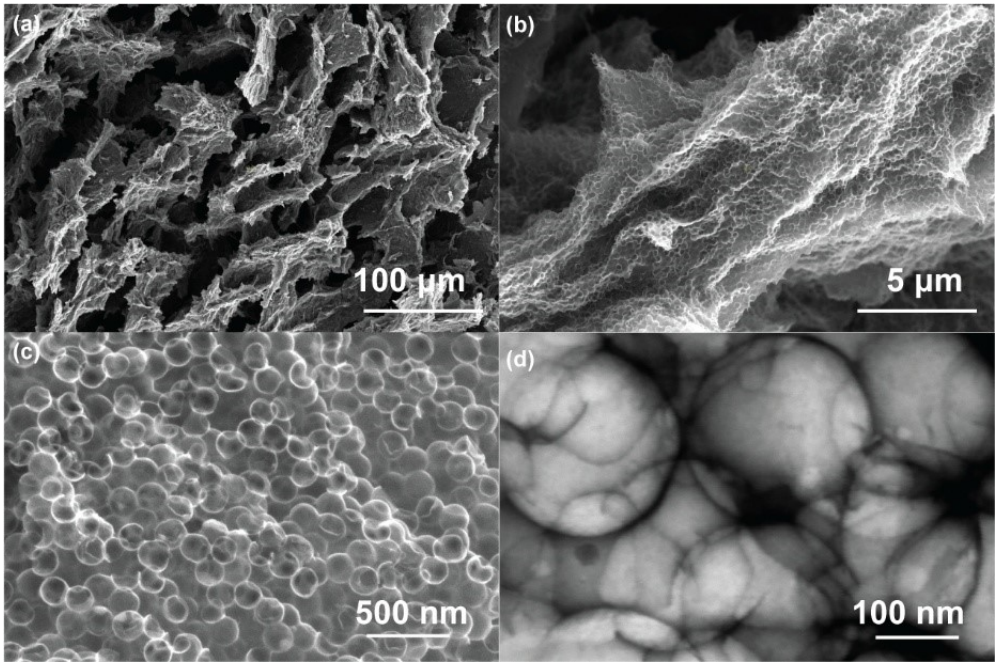

Figure S1. (a-c) SEM and (d) STEM images of MCA obtained at different magnifications.

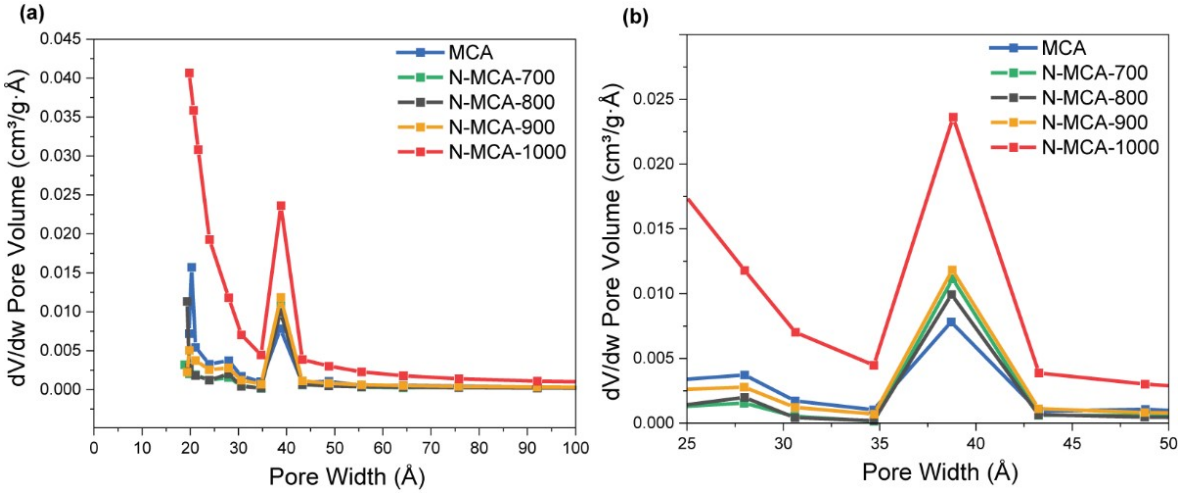

Figure S2. (a) Pore size distribution profile of MCA, N-MCA-700, N-MCA-800, N-MCA-900, and N-MCA-1000 calculated using Barrett-Joyner-Halenda (BJH) method. (b) Enlarged view of (a) showing the pore volume from 25 to 50 Å pore width.

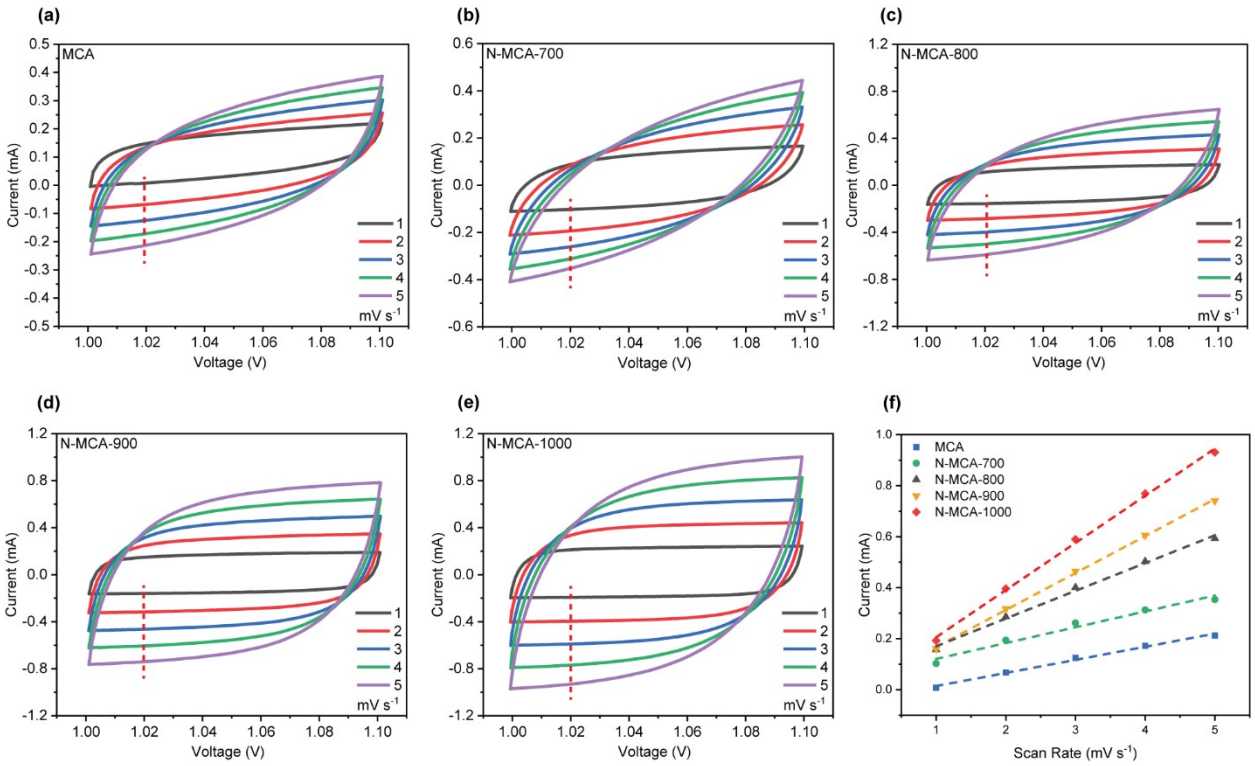

Figure S3. CV curves of (a) MCA and (b-e) N-MCAs measured at 20 °C. Dashed lines in the CV curves highlight the currents obtained at 1.02 V and different scan rates. (f) Cathodic currents obtained at 1.02 V are plotted as a function of scan rate. The dashed lines are linear fitting curves.

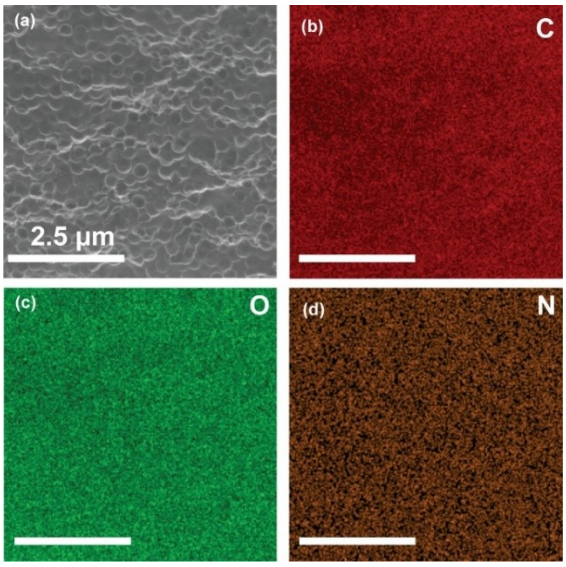

Figure S4. EDS maps of N-MCA-1000.

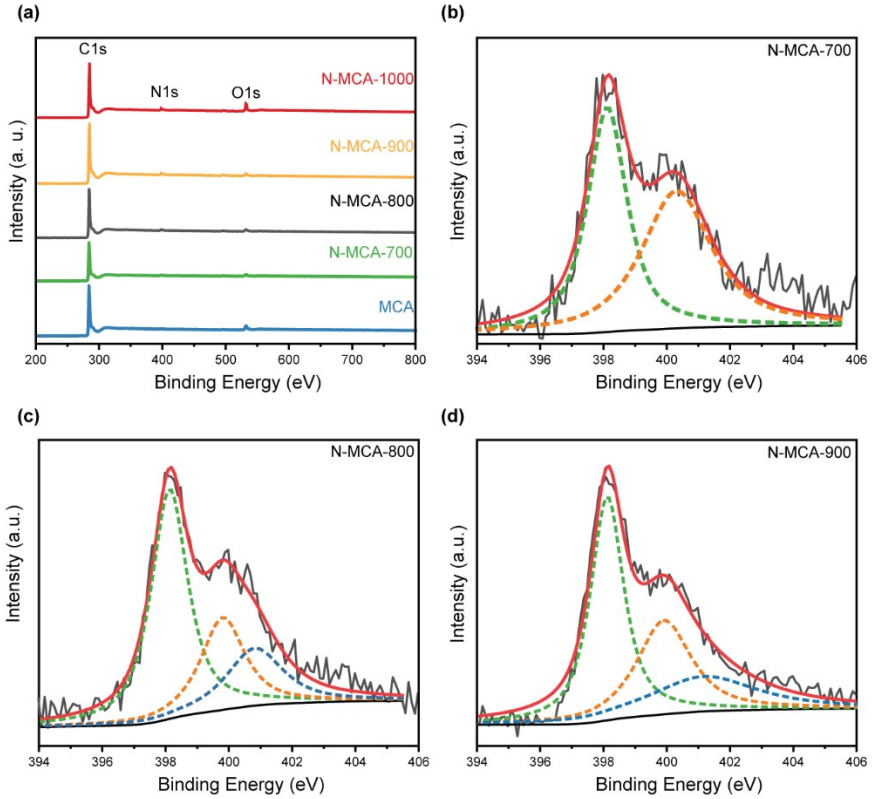

Figure S5. (a) XPS survey spectra of MCA and N-MCAs. N 1s core level XPS spectra of (b) N-MCA-700, (c) N-MCA-800, and (d) N-MCA-900. The dashed lines outline the deconvoluted peaks corresponding to pyridinic-N (green), pyrrolic-N (orange), and graphitic-N (blue).

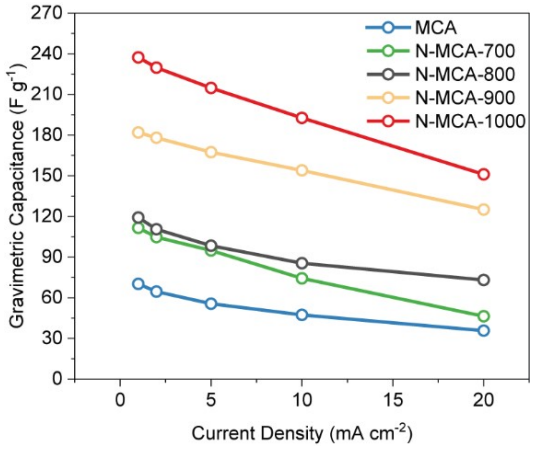

Figure S6. Gravimetric capacitance of MCA and N-MCAs measured in 0.5M $TEABF_4$ in 1:1 acetonitrile and methyl formate electrolyte using a three-electrode configuration, with carbon paper and platinum wire serving as the counter and reference electrodes, respectively.

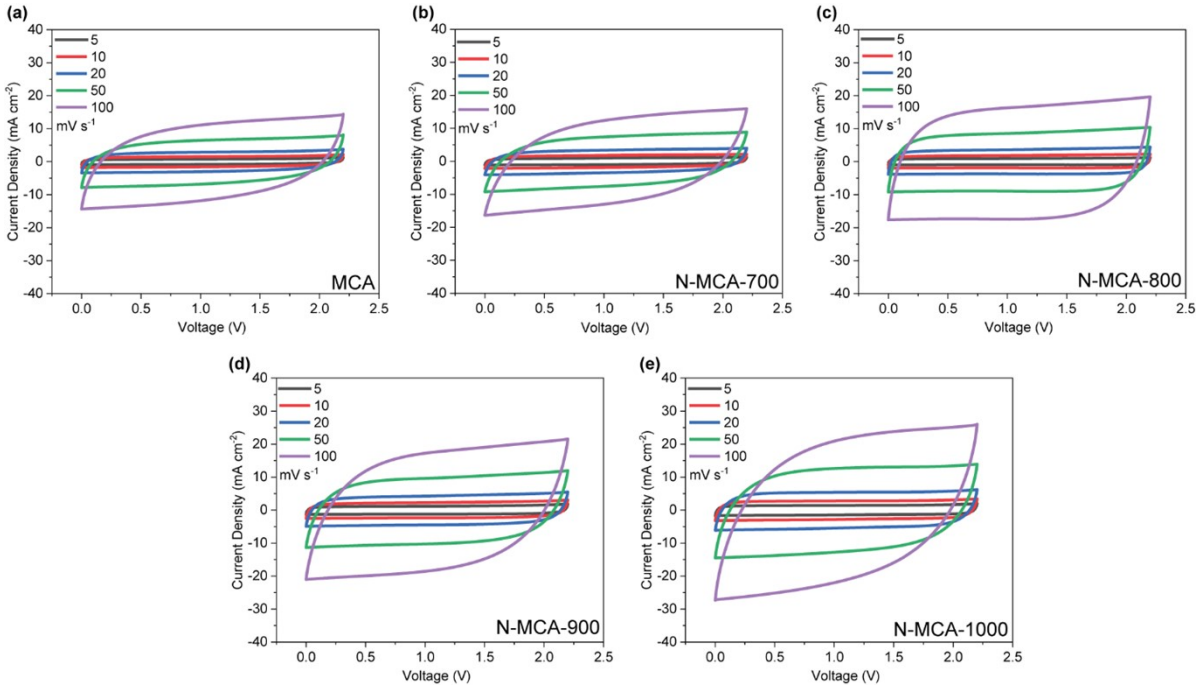

Figure S7. CV curves of symmetric supercapacitors, assembled with MCA and N-MCAs, and measured at 20°C.

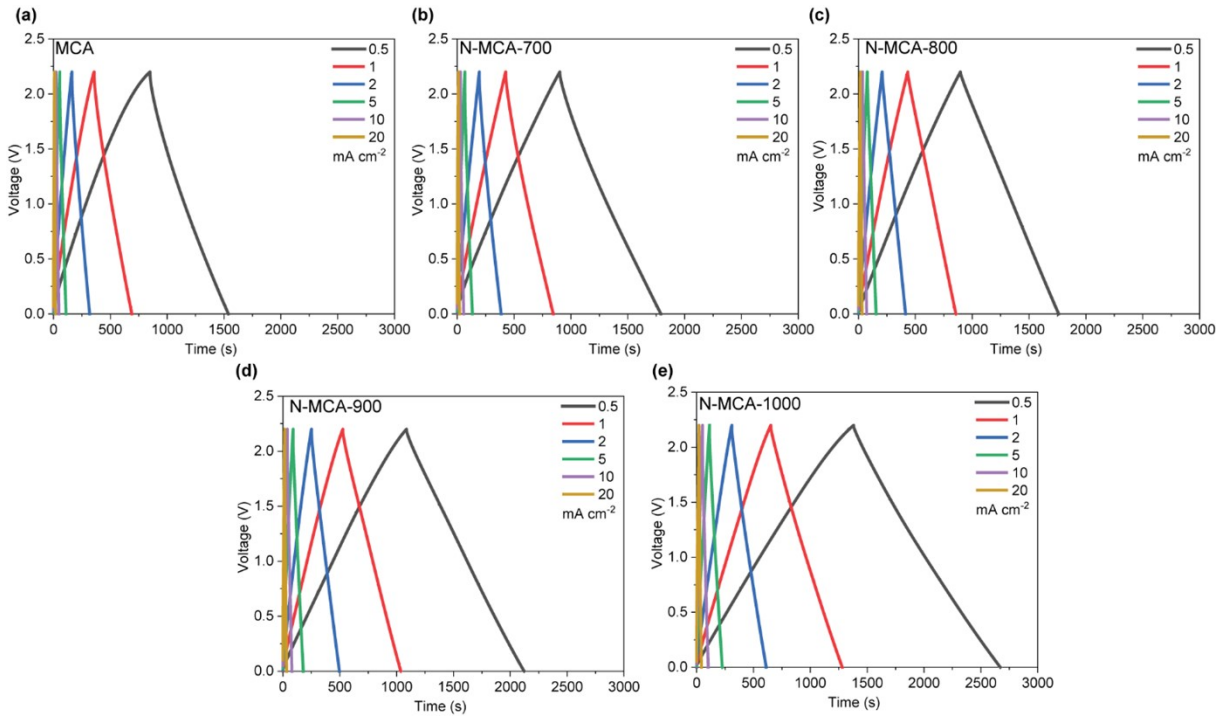

Figure S8. GCD curves of symmetric supercapacitors, assembled with MCA and N-MCAs, and measured at 20 °C.

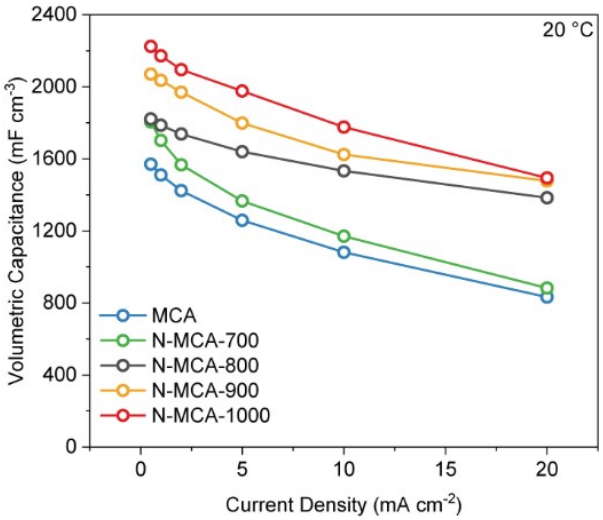

Figure S9. Volumetric capacitance of MCA and N-MCA devices as a function of current density at 20 °C.

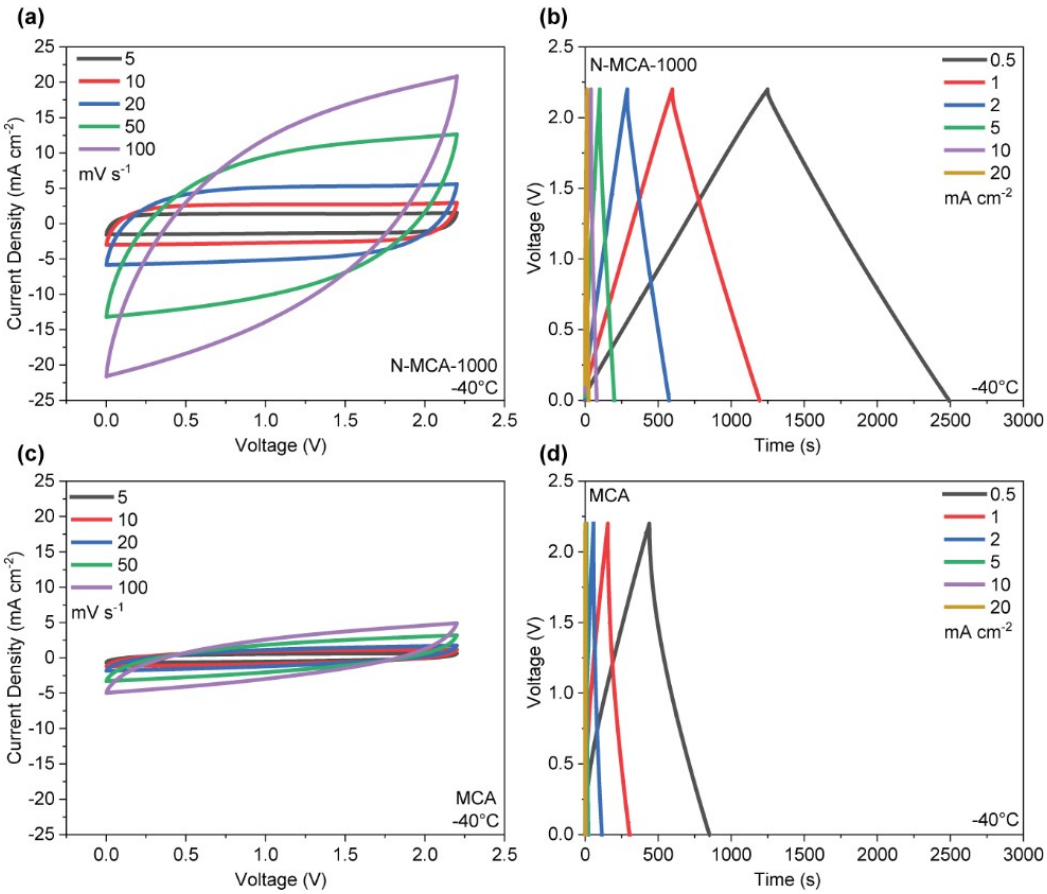

Figure S10. CV and GCD curves of symmetric supercapacitor devices assembled with N-MCA-1000 (a, b) and MCA (c, d) electrodes, collected at –40 °C.

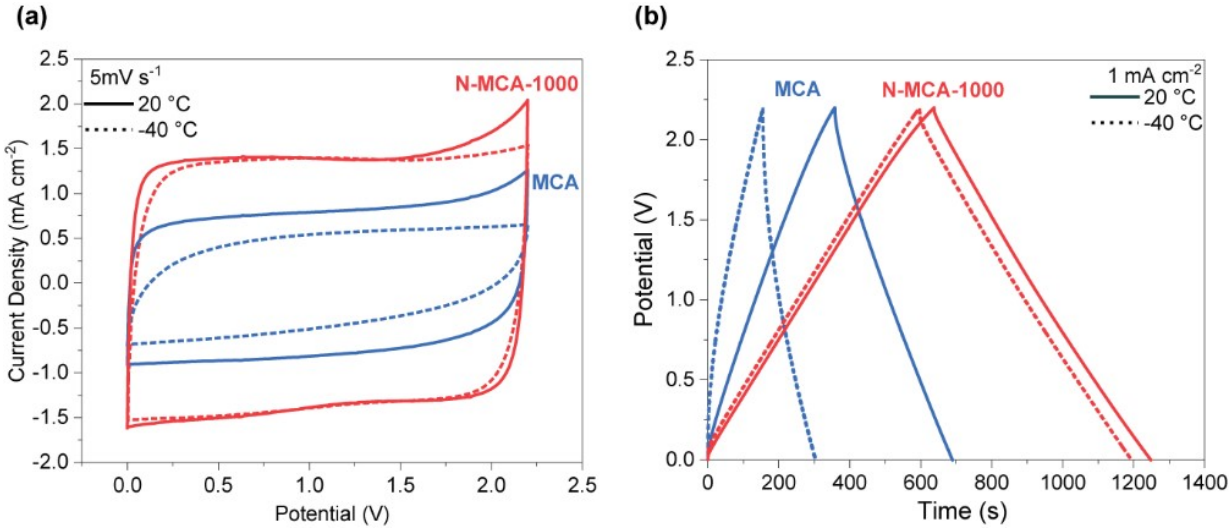

Figure S11. Comparing the (a) CV and (b) GCD curves of N-MCA-1000 and MCA devices at 20 °C and –40 °C.

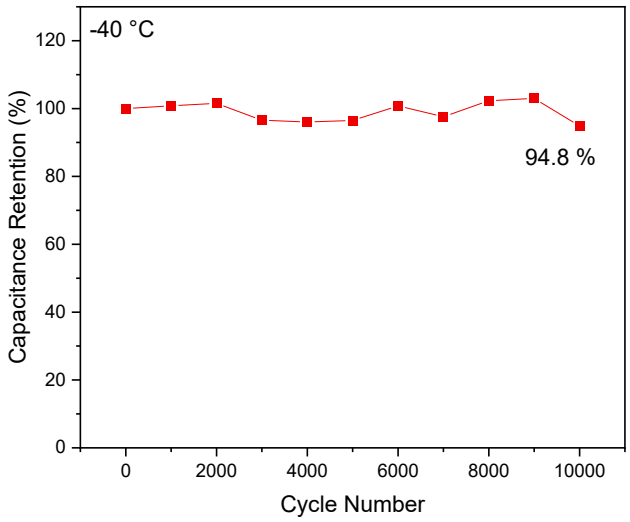

Figure S12. Capacitance retention of the N-MCA-1000 symmetric device measured in 1 M $TEABF_4$ in ACN/MF at -40 °C under a current density of 50 mA cm^{-2} for 10,000 cycles.

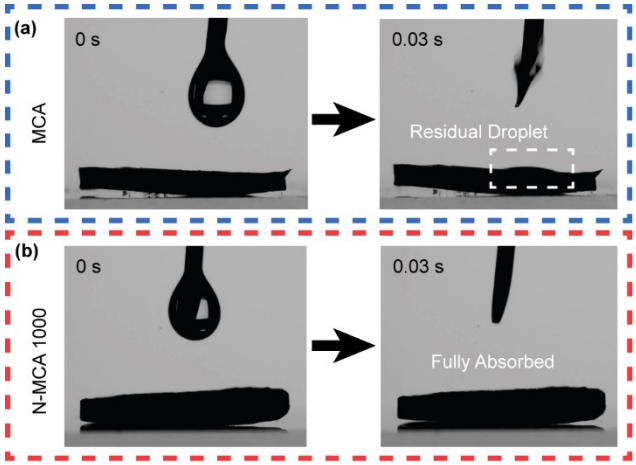

Figure S13. Contact angle measurements of (a) MCA and (b) N-MCA-1000.

According to Young's equation:

$$\gamma_{SL} = \gamma_{SV} - \gamma_{LV}cos\theta \qquad \text{Equation S1}$$

Where γ_{SL}, γ_{SV}, γ_{LV} are the surface tension of solid/liquid, solid/vapor and liquid/vapor interface, and θ is the contact angle.

Young's equation does not directly quantify ion adsorption; however, ion adsorption alters the solid-liquid interfacial energy, which in turn affects the contact angle. Therefore, a reduced contact angle serves as an indirect indicator of enhanced ion, surface interactions. The observed contact-angle difference between MCA and N-MCA-1000 is consistent with the expected N-doping-induced strengthening of ion adsorption.

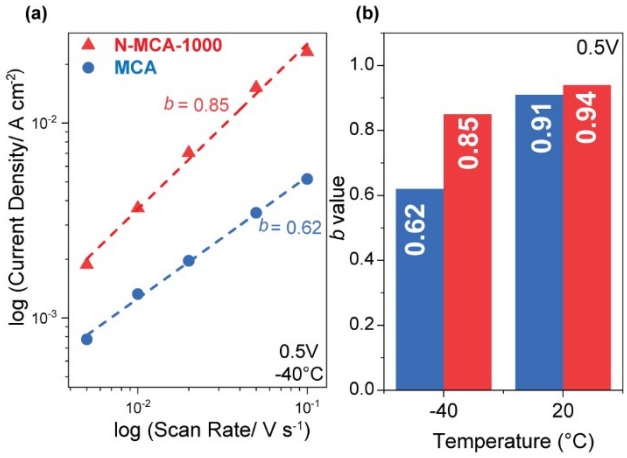

Figure S14. (a) Cathodic current densities of MCA and N-MCA-1000 at 0.5V vs. scan rate. (b) Comparison of *b* values at 0.5 V for N-MCA-1000 (red) and MCA (blue) at 20 °C and –40 °C.

Supplementary Table

Table S1. The electrochemical performance of representative supercapacitor devices using carbon-based electrodes at –40 °C.

Device	Electrolyte	Capacitance Retention Relative to room temp.	Ref.
Microwave exfoliated graphite oxide// Microwave exfoliated graphite oxide	PIP13-FSI/PPYR$_{14}$-FSI	70% @ 1 mV s^{-1}	5
N-doped graphene/carbon nanotube hydrogel// N-doped graphene/carbon nanotube hydrogel	37% H_2SO_4	90% @ 1mA cm^{-2}	6
Carbon fabric // Carbon fabric	37% H_2SO_4	83% @ 1mA cm^{-2}	7
MX-HGH2// MX-HGH2	37% H_2SO_4	71.1% @ 1mA cm^{-2}	8
3DP DQ/GC// 3DP PANI/GC	9.5 M H_3PO_4	66% @ 1mA cm^{-2}	9
3D WO_3/CNT/KB// 3D PBA/CNT/ KB	0.5M H_2SO_4 /ethylene glycol	64% @ 1mA cm^{-2}	10
3DP PDAN/CNT/rGO// 3DP PBA/CNT/rGO	9.5 M H_3PO_4	73% @ 2mA cm^{-2}	11
AC//AC	EG/Mg $(ClO_4)_2$	~56% @ 1 A g^{-1}	12
AC//AC	SBP-FSI/PC	~91% @ 0.1 A g^{-1}	13
AC@CNT-8//AC@CNT-8	0.5M $TEABF_4$ AN/DIOX	~84% @ 1 A g^{-1}	14
N-MCA-1000//N-MCA-1000	**0.5M $TEABF_4$ in AN/MF**	**96% @ 0.5 mA cm^{-2} 95% @ 1mA cm^{-2}**	**This Work**

References

1 B. Yao, H. Peng, H. Zhang, J. Kang, C. Zhu, G. Delgado, D. Byrne, S. Faulkner, M. Freyman, X. Lu, M. A. Worsley, J. Q. Lu and Y. Li, *Nano Lett.*, 2021, **21**, 3731–3737.

2 V. M. Masalov, N. S. Sukhinina, E. A. Kudrenko and G. A. Emelchenko, *Nanotechnology*, 2011, **22**, 275718.

3 S. Ardizzone, G. Fregonara and S. Trasatti, *Electrochimica Acta*, 1990, **35**, 263–267.

4 D. Baronetto, N. Krstajić and S. Trasatti, *Electrochimica Acta*, 1994, **39**, 2359–2362.

5 W.-Y. Tsai, R. Lin, S. Murali, L. Li Zhang, J. K. McDonough, R. S. Ruoff, P.-L. Taberna, Y. Gogotsi and P. Simon, *Nano Energy*, 2013, **2**, 403–411.

6 S. Liang, L. Sun, J. Liao, Y. Huang, N. Wang and W. Hu, *Ionics*, 2025, **31**, 6191–6203.

7 M. Xiang, J. Liao, N. Wang, L. Sun, L. He, X. Xie, S. Komarneni, G. Imanova and W. Hu, *Chemical Engineering Journal*, 2024, **501**, 157620.

8 Q. Su, C. Lin, M. Xiang, N. Wang, L. Sun and W. Hu, *J Solid State Electrochem*, 2024, **28**, 3263–3274.

9 M. Zhang, T. Yao, T. Xu, X. Zhou, D. Chen and L. Shen, *Advanced Functional Materials*, 2025, **35**, 2413436.

10 M. Zhang, T. Xu, D. Wang, T. Yao, Z. Xu, Q. Liu, L. Shen and Y. Yu, *Advanced Materials*, 2023, **35**, 2209963.

11 M. Zhang, T. Yao, T. Xu, X. Zhou, D. Chen and L. Shen, *Advanced Powder Materials*, 2025, **4**, 100247.

12 G. Tian, P. Chai, H. Yu and W. Zheng, *J Solid State Electrochem*, 2023, **27**, 2771–2777.

13 W. Zhang, J. Wang, D. Ruan, Q. Shi, F. Zhang, Q. Ren and Z. Shi, *Chemical Engineering Journal*, 2019, **373**, 1012–1019.

14 J. Xu, X. Wang, X. Zhou, N. Yuan, S. Ge and J. Ding, *Electrochimica Acta*, 2019, **301**, 478–486.

15 G. J. Brug, A. L. G. van den Eeden, M. Sluyters-Rehbach and J. H. Sluyters, *Journal of Electroanalytical Chemistry and Interfacial Electrochemistry*, 1984, **176**, 275–295.

16 A. Ch. Lazanas and M. I. Prodromidis, *ACS Meas. Sci. Au*, 2023, **3**, 162–193.

17 B.-A. Mei, J. Lau, T. Lin, S. H. Tolbert, B. S. Dunn and L. Pilon, *J. Phys. Chem. C*, 2018, **122**, 24499–24511.